Research Square

Preprints are preliminary reports that have not undergone peer review.
They should not be considered conclusive, used to inform clinical practice,
or referenced by the media as validated information.

Targeting the HSP90β/VEGFR2 Axis in Radiation-Induced Brain Injury: the Novel Inhibitor KDR2-2 Ameliorates Neurovascular Dysfunction

Jingwen Yang
Sun Yat-sen Memorial Hospital
Xia Hu
Sun Yat-sen Memorial Hospital
Kejia Liu
Sun Yat-sen Memorial Hospital
Haiyu Zhong
Sun Yat-sen Memorial Hospital
Xiaoqiu Zhu
Sun Yat-sen Memorial Hospital
You Zuo
Sun Yat-sen Memorial Hospital
Sitai Chen
Sun Yat-sen Memorial Hospital
Shaojian Li
Sun Yat-sen Memorial Hospital
Zhenhong Deng
Sun Yat-sen Memorial Hospital
Xiaolu Liu
Sun Yat-sen Memorial Hospital
Qing Liu
Sun Yat-sen Memorial Hospital
Xueying Ma
Sun Yat-sen Memorial Hospital
Yongteng Xu
Sun Yat-sen Memorial Hospital
Zhongshan Shi
Sun Yat-sen Memorial Hospital
Yamei Tang
tangym@mail.sysu.edu.cn

Sun Yat-sen Memorial Hospital

Research Article

Keywords: radiation-induced brain injury, Vascular endothelial growth factor receptor 2, Heat shock protein 90, Phosphorylation, Tyrosine kinase inhibitor

Posted Date: October 23rd, 2026

DOI: https://doi.org/10.21203/rs.3.rs-11243407/v1

License: This work is licensed under a Creative Commons Attribution 4.0 International License.
Read Full License

Additional Declarations: No competing interests reported.

Targeting the HSP90β/VEGFR2 Axis in Radiation-Induced Brain Injury: the Novel Inhibitor KDR2-2 Ameliorates Neurovascular Dysfunction

Jingwen Yang[1,2,7], Xia Hu[1,2,7], Kejia Liu[1,2,7], Haiyu Zhong[1,2,7], Xiaoqiu Zhu[3], You Zuo[1,2], Sitai Chen[1,2], Shaojian Li[1,2], Zhenhong Deng[1,2], Xiaolu Liu[1,2], Qing Liu[1,2], Xueying Ma[1,2], Yongteng Xu[1,2*], Zhongshan Shi[1,2,4,5*], and Yamei Tang[1,2,4,5,6,8*]

Abstract

Background: Radiation-induced brain injury(RIBI) is one of the most common complications of cranial radiotherapy. While the VEGF antagonist bevacizumab has been the therapeutic mainstay for RIBI, its efficacy is often limited by drug resistance and high recurrence rates. These limitations underscore the imperative for novel therapeutic strategies.

Methods: This study evaluates the therapeutic potential of KDR2-2, a novel and potent VEGFR2 inhibitor, in a murine model of Gamma Knife-induced RIBI. We compared its efficacy against bevacizumab and utilized bulk RNA sequencing and high-throughput phosphoprotein profiling to elucidate the underlying molecular mechanisms.

Results: KDR2-2 demonstrated superior efficacy over bevacizumab in reducing brain lesion, restoring vascular perfusion, and normalizing vessel morphology. Furthermore, KDR2-2 treatment significantly mitigated astrocyte-mediated neuroinflammation and reduced neuronal loss. Mechanistic analysis revealed that radiation triggers specific phosphorylation of VEGFR2 at Y1214 and HSP90β at S226, distinct from the canonical phosphorylation sites associated with physiological angiogenesis. We further demonstrate that HSP90β drives VEGFR2 Y1214 phosphorylation via a non-canonical, VEGFA-independent pathway. Consequently, depleting HSP90β significantly attenuated radiation-induced VEGFR2 activation.

Conclusions: These findings identify the HSP90β–VEGFR2 Y1214 signaling axis as a unique and critical driver of neurovascular dysfunction in RIBI. KDR2-2 targets this pathological mechanism more effectively plus ligand-based inhibition, suggesting it is a promising therapeutic candidate for patients refractory to current anti-VEGF therapies.

Author affiliations:

[1]Department of Neurology, Sun Yat-Sen Memorial Hospital, Sun Yat-Sen University, Guangzhou 510120, China

[2]Brain Research Center, Sun Yat-Sen Memorial Hospital, Sun Yat-Sen University, Guangzhou 510120, China

[3]Department of Anesthesiology, Sun Yat-Sen Memorial Hospital, Sun Yat-Sen University, Guangzhou 510120, China

[4]Nanhai Translational Innovation Center of Precision Immunology, Sun Yat-Sen Memorial Hospital, Foshan 528200, China

[5]Guangdong Provincial Key Laboratory of Malignant Tumor Epigenetics and Gene Regulation, Guangdong-Hong Kong Joint Laboratory for RNA Medicine, Medical Research Center, Sun Yat-Sen Memorial Hospital, Sun Yat-Sen University, Guangzhou 510120, China

[6]Sun Yat-sen University School of Medicine, Sun Yat-sen University, Shenzhen 518107, China

[7]These authors contributed equally

[8]Lead contact

Correspondence to:

Yamei Tang

Director, Brain Research Center; Professor and Chair, Department of Neurology

Sun Yat-sen Memorial Hospital, Sun Yat-sen University

107 West Yan Jiang Rd.

Guangzhou 510120

China

E-mail: tangym@mail.sysu.edu.cn

Zhongshan Shi

Department of Neurology

Sun Yat-sen Memorial Hospital, Sun Yat-sen University

107 West Yan Jiang Rd.

Guangzhou 510120

China

E-mail: shizhsh@mail.sysu.edu.cn

Yongteng Xu

Department of Neurology

Sun Yat-sen Memorial Hospital, Sun Yat-sen University

107 West Yan Jiang Rd.

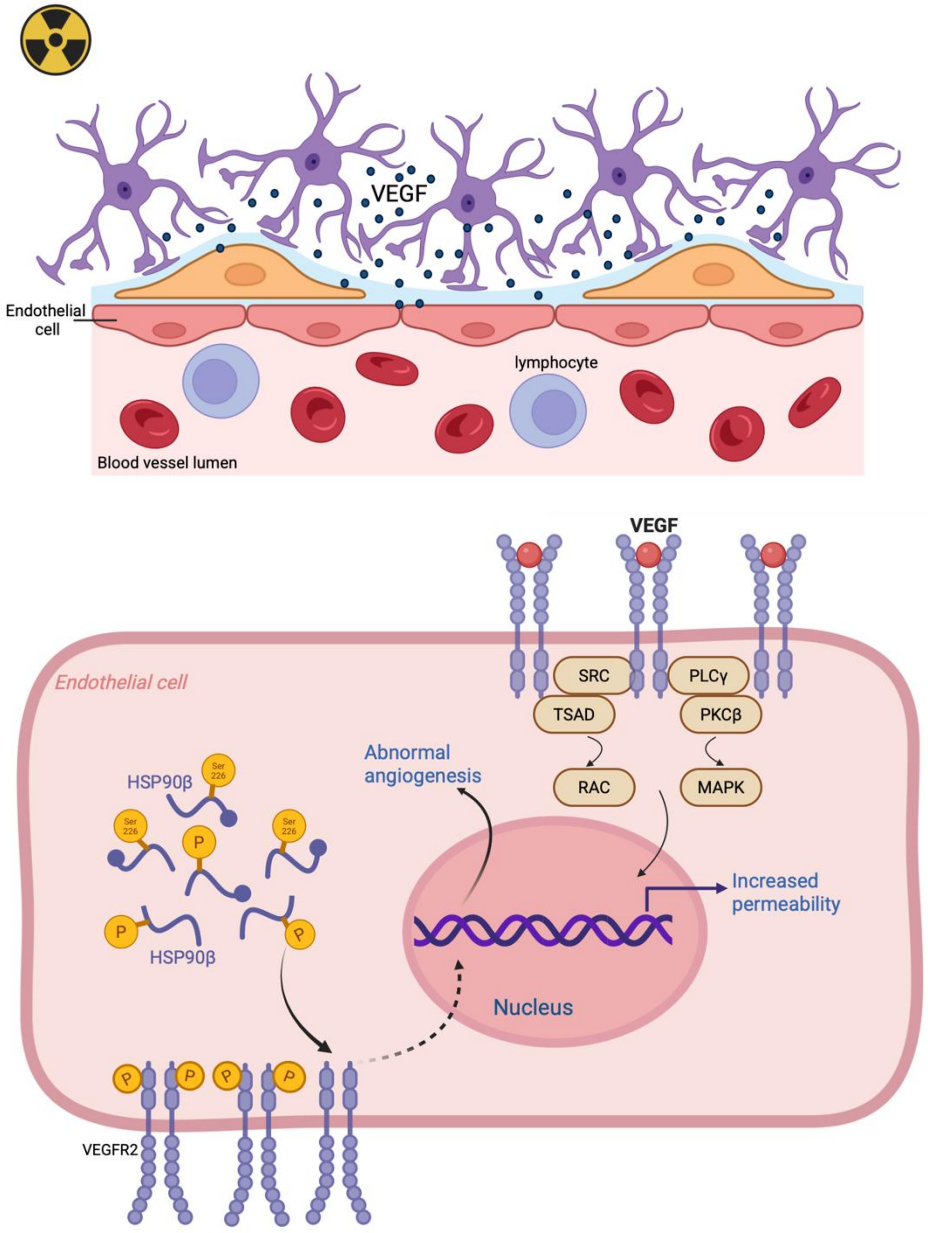
Guangzhou 510120

China

E-mail: xuyt5@mail2.sysu.edu.cn

Running title: Targeting HSP90β/VEGFR2 in Radiation-Induced Brain Injury

Key words: radiation-induced brain injury; Vascular endothelial growth factor receptor 2; Heat shock protein 90; Phosphorylation; Tyrosine kinase inhibitor.



Graphical Abstract

Introduction

Cranial radiotherapy is a mainstay therapeutic modality for various primary and metastatic head and neck tumors[1-2]. However, as radiation fields inevitably encompass neural tissues,

radiation-induced brain injury (RIBI) remains a critical complication[3-4]. Late-onset RIBI presents a significant clinical challenge due to its insidious progression and the development of irreversible symptoms, including cognitive impairment and focal cerebral necrosis[5].

Radiation-induced vascular injury impairs oxygen diffusion, causing tissue hypoxia and subsequent stabilization of HIF-1α[6]. Aberrant accumulation of HIF-1α stimulates activated astrocytes to release VEGF, promoting the formation of disorganized neovessels [7]. These pathological vessels exhibit markedly heightened permeability, resulting in plasma extravasation and aggravated cerebral edema, which raises local intracranial pressure[8]. This elevated pressure exacerbates ischemia and hypoxia, establishing a vicious feedback that ultimately progresses to radiation necrosis [8].

Bevacizumab, a recombinant humanized monoclonal antibody, binds VEGF and prevents its interaction with vascular endothelial growth factor receptor 2 (VEGFR2). While this effectively suppresses pathological angiogenesis, improves endothelial barrier function, and alleviates cerebral edema, its efficacy is limited[9]. Bevacizumab primarily targets vessels surrounding the necrotic area and modulates edema formed by new vessels, but it does not reverse necrosis itself[9]. Consequently, local hypoxia and ischemia persist if the underlying necrotic pathology remains unresolved[9]. Upon discontinuation, HIF-1α expression often rebounds, reigniting the vicious cycle and leading to recurrence[9]. Furthermore, long-term treatment significantly increases the risk of drug resistance, rendering re-treatment ineffective and leaving patients with few therapeutic alternatives[10].

The clinical utility of anti-VEGF antibodies is further hampered by issues of immunogenicity, instability, and the inhibition of physiological angiogenesis[11]. Direct VEGFR inhibition has therefore emerged as a potentially more effective strategy than ligand targeting for suppressing tumor angiogenesis[12]. In a study of 36 patients with nasopharyngeal carcinoma-related RIBI, apatinib (250mg daily) yielded a ≥25% reduction in cerebral edema volume in 61.1% of patients—a response rate comparable to the 50%–65.5% reported for bevacizumab[13]. However, other clinical studies investigating alternative tyrosine kinase inhibitors(TKIs) for RIBI have been limited by small sample sizes, short follow-up periods, and a lack of supporting basic research[13,14].

Different TKIs exhibit varying inhibitory potency and selectivity toward VEGFR2 [15]. VEGFR2 activation—a prerequisite for its function—occurs through both canonical (VEGF-dependent) and non-canonical (VEGF-independent) pathways, involving phosphorylation at multiple tyrosine residues[16,17]. Beyong Y1054 and Y1059, which are essential for its kinase activity, key phosphorylation sites include Y951 (Y949 in mice), Y1175 (Y1173 in mice), and Y1214 (Y1212 in mice). Upon phosphorylation, these sites recruit distinct intracellular adaptor proteins to transduce VEGFA signaling[18,19].

Phosphorylation at specific VEGFR2 residues mediates distinct pathological processes. In hypoxic pulmonary hypertension, the VEGFA/VEGFR2 Y949 axis drives vascular leakage, a process prevented by a Vefgr2 Y949F mutation[20]. In renal cell carcinoma, VEGFR2 pY1173/PLCγ signaling promotes vascular leakage by inducing VE-cadherin Y685 phosphorylation, which is stabilized in Vegfr2 Y1173F/+ or Plcg1iECKO mice[21]. Additionally, VEGFR2 Y1214 is essential for SAPK2/p38-mediated actin remodeling[22]. In hypertensive models, GPCR-activated MSK1 can trigger VEGFR2 Y1173 phosphorylation independently of VEGFA[23].

Consequently, site-specific VEGFR2 phosphorylation drives diverse disease pathologies. Elucidating these distinct mechanisms holds promise for refining treatment strategies for RIBI. In this study, we evaluate KDR2-2, a novel and potent VEGFR2 antagonist, in a murine model of RIBI, and demonstrate its superior efficacy over the current standard-of-care bevacizumab in reducing brain lesions, restoring vascular perfusion, and mitigating neuroinflammation. Mechanistically, we identify a non-canonical HSP90β-driven VEGFR2 Y1214 phosphorylation axis that critically mediates radiation-induced neurovascular dysfunction, revealing a distinct pathological mechanism that can be therapeutically targeted.

Materials and Methods

1. Animals and Drug Administration

Male wild-type C57BL/6 mice (7-9 weeks old, weighing 20-25g) were purchased from Zhuhai BaiShiTong Biotechnology Co., Ltd. and housed under specific-pathogen-free (SPF) conditions with a maximum of 5 mice per cage. The facility maintained a 12-hour light/dark cycle with appropriate temperature and humidity. Food and water were provided *ad libitum*. All experimental procedures were approved by the Sun Yat-sen University Animal Research Ethical Committee (SYSU-IACUC-2024-002988) and followed the NIH Guide for the Care and Use of Laboratory Animals. Every effort was made to minimize animal suffering and usage.

KDR2-2 (Guangzhou Huibairui Pharmaceutical Co. Ltd., Guangzhou, China) and bevacizumab (Avastin, Roche Holding AG, Swizerland) were used for treatment. Dosing regimen were based on published literature, manufacturer recommendations, and our preliminary data[24]. Specifically, bevacizumab (10 mg/kg), KDR2-2 (40 mg/kg), or an equivalent volume of vehicle (saline) was administered intraperitoneally twice weekly for 8 weeks, starting from the first week post-irradiation. Magnetic resonance imaging (MRI) was performed at week 8 to evaluate lesion changes, after which mice were sacrificed for analysis.

Clinical trial number: not applicable. This study is a preclinical investigation. The compound KDR2-2 has been evaluated in two registered clinical trials (NCT04620109, registered on 6th November 2020; NCT04844619, registered on 14th April 2021); however, these registrations do not apply to the present study.

2. Gamma Ray irradiation

To replicate clinical RIBI, mice underwent unilateral thalamic gamma ray irradiation as previously described[25,26]. Briefly, anesthetized mice were immobilized in a prone position on a Leksell stereotactic frame (Model G) equipped with a CT fiducial indicator box. Brain CT imaging was performed (GE Revolution CT; 80 kV; slice thickness/interval: 0.625 mm; FOV: 195 mm; matrix: 512 × 512). The images were imported into Leksell GammaPlan (v10.2),

and a 4-mm collimator was used to target the coordinates (AP: -2 mm, L: 2 mm, DV: 2 mm relative to bregma and dura). Irradiation was delivered using a Leksell Gamma Knife® Perfexion™.

3. Magnetic resonance imaging (MRI)

MRI was performed at 8 weeks post-irradiation using a 7.0-T small-animal MR scanner (Bruker Biospin MRI GmbH) with Paravision 6.0 operating system. Anesthesia was induced with 3% (vol/vol) isoflurane/O_2 and maintained with 1% (vol/vol) isoflurane/O_2 throughout the procedure. Mice were restrained in a custom-built head holder, and body temperature was maintained at approximately 37 °C using a circulating warm-water pad. All images were acquired immediately following an intraperitoneal injection of the Omniscan contrast agent (Gadoteric Acid Meglumine Salt Injection, Magnevist) at a concentration of 50 mg/mL.

4. Quantitative Assessment of Necrotic Volumes by MRI Imaging

Necrotic volumes were quantified based on T1-weighted images using the open-source ITK-SNAP software, following the developer's protocol. Regions of interests (ROIs) were manually delineated across contiguous slices encompassing the entire brain, with a focus on the hyperintense foci in the irradiated left hemisphere. The final necrotic volume was determined through iterative contrast adjustment by gradually modifying the threshold, coupled with stepwise loading of the segmentation image files.

5. Cerebral Blood Flow Assessment

Following anesthesia with 4% isoflurane, mice were positioned prone under the probe and monitored for 3 minutes. ROIs were located in over the somatosensory cortex. Cerebral perfusion was assessed and quantified using Perimed PSI-ZR blood flow imaging software (Perimed PSI, Jarfalla, Sweden).

6. Bulk RNA sequencing

With approval from the Sun Yat-sen University Institutional Review Board and patients informed consent, clinical data were collected from 2019 to 2023 at Sun Yat-sen Memorial Hospital. Samples were from the necrotic peripheral area of RIBI and relatively normal brain

tissue removed for surgical approaches of other neurological diseases (patient characteristics in Table S1).

Human brain tissue and mouse ipsilateral thalamus were subjected to bulk RNA-seq. RNA quantity and integrity were assessed using the RNA Nano 6000 Assay Kit on a Bioanalyzer 2100 system (Agilent Technologies, CA, USA). Libraries were prepared with the NEBNext® Ultra™ Directional RNA Library Prep Kit for Illumina® (NEB, USA) and clustered using the TruSeq PE Cluster Kit v3-cBot-HS (Illumina, USA) , then quantified and qualified. Sequencing was performed on an Illumina NovaSeq 6000, generating 150 bp paired-end reads. Raw FASTQ data were processed with in-house Perl scripts to remove adapter, ploy-N, and low-quality reads, yielding clean reads, which were aligned to hg19 and quality-checked by FASTQC. Gene expression was quantified as Fragments Per Kilobase of transcript sequence per Millions base pairs sequenced (FPKM). Differential expression analysis used DESeq2 with Benjamini-Hochberg correction; DEGs were defined as padj<0.05 & |log2(foldchange)|>1. Scatter plots of top DEGs were created using ggplot2 v2.2.1 in R. A heatmap of phosphorylation-related genes was generated after batch correction and sorting by relative expression change.

7. Phosphoprotein Profiling

Phosphoprotein Profiling was performed using the Phospho Explorer Array CSP100 plus kit. Briefly, cell lysates from bEND.3 with or without radiation were biotinylated with Antibody Array Assay Kit (Full Moon Biosystems, Inc.). Antibody microarray slides were blocked, rinsed, dried with compressed nitrogen, and then incubated with biotin-labeled cell lysates (~100μg protein) in coupling solution for 2 h at room temperature. Bound proteins were detected with Cy3-streptavidin. Slides were scanned on a GenePix 4000 scanner (Axon, USA) and analyzed with GenePix Pro 6.0 (Molecular Devices, Sunnyvale, CA). The phosphorylation ratio for each antibody was calculated as the phosphorylated signal divided by the corresponding unphosphorylated signal. Results are provided in Supplementary Table 2.

8. Cell Culture and Transfection

bEND.3 (mouse cerebral microvascular endothelial cell line) cells were cultured in

DMEM medium (Gibco, C11330500BT) containing 10% fetal bovine serum (Gibco, 10099141C). A single dose of 10 Gy X-ray radiation was applied[27-29]. Cells were pretreated with 10 μM apatinib, cabozantinib, KDR2-2 or vehicle (equal volume of DMSO) for 1 h before irradiation[30]. After irradiation, cells were maintained in complete medium for 24 h before protein extraction and analysis.

Hsp90β siRNA (*siHsp90β*) and negative control siRNA (*siNC*) were synthesized by OBiO Biotechnology Co., Ltd. bEND.3 cells were transfected with the *siRNAs* using Lipofectamine™ 3000 (Invitrogen) according to the instructions and were used 24 h post-transfection. *siRNA* sequences are listed in Table S2.

9. Immunofluorescence

Mice were transcardially perfused with 0.9% saline and fixed with pre-cooled 4% paraformaldehyde (PFA) in 0.1 M phosphate buffer (pH 7.4). Brains were post-fixed in 4% PFA for 1-2 h, cryopreserved in 20% and 30% sucrose at 4°C, embedded in OCT, and sectioned at 20 μm. For immunofluorescence, sections were blocked with 5% bovine serum albumin (BSA; MRC, USA) and 0.3% Triton X-100 (Sigma-Aldrich, USA) for 1h at room temperature, then incubated overnight at 4 °C with primary antibodies: rabbit anti-GLUT1 (1:500, Invitrogen, SA0377), mouse anti-GFAP (1:500, CST, 3670S), rabbit anti-Iba1 (1:200, Wako, 019-19741), rabbit anti-NeuN (1:100, CST, 24307S), rabbit anti-CD31 (1:50, Abcam, ab28364), and rabbit anti-Fibrinogen (1:100, Abcam, ab281924). After washing, sections were incubated with Alexa Fluor-coupled secondary antibodies (1:500, Abcam, ab150153) for 1h at room temperature, mounted with Fluoroshield containing DAPI (Sigma, F6057), and imaged by fluorescence microscope (Leica DM6B, Germany).

10. Western Blotting

Mouse ipsilateral thalamus was collected 8 weeks post-irradiation and stored at -80°C. Brain tissues or cells were lysed in RIPA lysis buffer (P0013B, Beyotime) on ice for 20 min, centrifuged (15,000 rpm, 15 min, 4 °C), and the supernatants collected. Protein concentrations were determined by BCA Assay Kit (23227, Thermo Scientific). Protein were resolved on 8% SDS-PAGE gels, transferred to PVDF membranes, and blocked with 5% non-fat milk.

Membranes were incubated overnight at 4 °C with primary antibodies: rabbit anti-VEGFR2 (1:1000, CST, 9698S), rabbit anti-VEGFR2 pY951 (1:1000, CST, 4991S), rabbit anti-VEGFR2 pY1175 (1:1000, CST, 3770S) , rabbit anti-VEGFR2 pY1214 (1:1000, Immunoway, YP0111), rabbit anti-VEGFR2 pY1054 (1:1000, Abmart, PA5881S), rabbit anti-VEGFR2 pY996 (1:1000, CST, 2474T), rabbit anti-Hsp90β pS226 (1:2000, Affinity, AF7210), anti-Hsp90β (1:2000, Abcam, Ab32568), rabbit anti-β actin (1:5000, Protein tech, 81115-1-RR), and mouse anti-α actinin (1:5000, Protein tech, 66895-1-IG). After washing with TBST three times, the membranes were incubated with secondary antibodies at room temperature for 1 h. The secondary antibodies include HRP-conjugated Goat Anti-Rabbit IgG (1:5000, Protein tech, SA00001-2) and HRP-conjugated Goat Anti-Mouse IgG (1:5000, Protein tech, SA00001-1). Detection was performed using the Odyssey Infrared Imaging System (LI-COR Biosciences, Lincoln, NE, USA), and the bands were quantified by ImageJ software.

11. RNA Extraction and Quantitative Real-time PCR analysis

Total RNA was extracted from cells using the RNA Easy Fast Cell Total RNA Kit (GOONIE, 400-100-1kit) and reverse transcribed into complementary DNA (cDNA) with PrimeScript RT Master Mix (TakaRa, RR036A). Real-time quantitative PCR (RT-qPCR) was performed on a CFX96 Touch System (BioRad) using TB Green Premix Ex Taq II (TakaRa, RR820A). Relative expression for each target gene was calculated as the $2^{-\Delta\Delta CT}$ value after normalization to GAPDH. Primers sequences are listed in Supplementary Table 3.

12. Statistical Analysis

Statistical analyses were performed using GraphPad prism 9.0 software (GraphPad Software, San Diego, CA). Normality of continuous variables was assessed by the Shapiro-Wilk test; all data passed normality and equal variance. Unpaired Student's t-test was used for two-group comparisons, and one-way ANOVA with Tukey's multiple comparisons test was applied for three or more groups. Data are presented as means ± SEM, with $P<0.05$ considered significant. No data were excluded. Sample ID was blinded to the investigator for image quantification.

Results

1. KDR2-2 attenuates necrotic lesion size, ameliorate blood flow recovery and improve vascular network formation after radiation

To evaluate the differential inhibitory effects of VEGFR2 by various TKIs, irradiated bEND.3 cells were treated with equimolar concentrations of apatinib, cabozantinib, or KDR2-2. Apatinib treatment showed no apparent suppressive effect compared to the radiation group (Supple Fig. 1A). In contrast, KDR2-2 potently suppressed VEGFR2 expression, showing a significant reduction relative to both the radiation group (Supple Fig. 1B, P=0.0012) and the apatinib-treated group (Supple Fig. 1B, P=0.0003). Cabozantinib induced a mild, statistically insignificant decrease in VEGFR2 (Supple Fig. 1C, D; P=0.5509). Notably, KDR2-2 achieved a significantly greater suppression than cabozantinib (Supple Fig. 1C, D; P=0.005).

Based on the superior efficacy of KDR2-2 in inhibiting VEGFR2 in vitro, we evaluated its therapeutic potential against RIBI in mice compared to Bevacizumab (Fig. 1A). Following Gamma Knife irradiation, mice received vehicle, Bevacizumab, or KDR2-2. MRI at 8 weeks revealed contrast-enhancing RIBI lesions (Fig. 1B). Quantitative analysis demonstrated that both Bevacizumab and KDR2-2 significantly reduced lesion size and edema versus vehicle (Fig. 1C, P=0.0089 and P<0.0001, respectively), with KDR2-2 exhibiting a significantly greater therapeutic effect than Bevacizumab (Fig. 1C).

Radiation-induced microvascular pathology, including dilation, rarefaction, occlusion, and structural rigidity, promotes cerebral hypoperfusion and ischemic injury[31-36]. We therefore assessed whether KDR2-2 improves cerebral perfusion and vascular structure in RIBI. Laser speckle imaging (LASCA) revealed severely impaired cortical perfusion in Vehicle-treated irradiated mice (Fig. 1D). Bevacizumab significantly improved perfusion versus Vehicle (Fig. 1E, P<0.0001), an effect surpassed by KDR2-2 (Fig. 1E, P<0.0001).

Immunofluorescence staining of GLUT1-labeled endothelium showed decreased vascular density and increased diameter in Vehicle-treated mice (Fig. 1F). Quantification confirmed severe rarefaction and dilation after irradiation (Fig. 1G, P<0.0001). Bevacizumab partially restored density (Fig. 1G, P=0.0313), while KDR2-2 showed stronger restoration (Fig. 1G,

P<0.0001). Both agents significantly reduced pathological vessel dilation versus Vehicle (Fig. 1H, P<0.0001), with no significant difference between them.

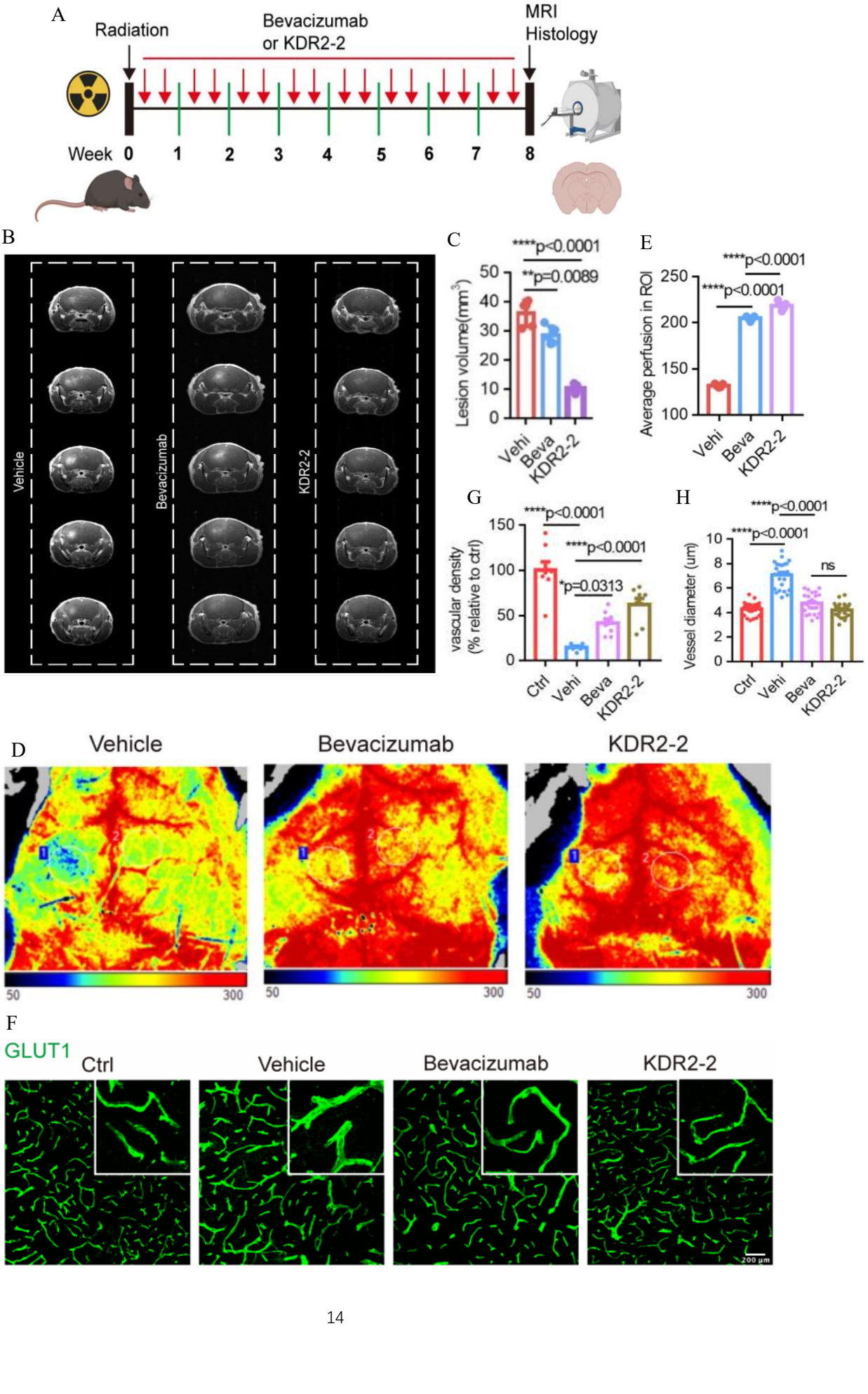

A
Radiation
Bevacizumab
or KDR2-2
MRI
Histology
Week 0 1 2 3 4 5 6 7 8
B
Vehicle
Bevacizumab
KDR2-2
C
****p<0.0001
**p=0.0089
Lesion volume(mm3)
Vehi
Beva
KDR2-2
E
****p<0.0001
****p<0.0001
Average perfusion in ROI
Vehi
Beva
KDR2-2
G
****p<0.0001
****p<0.0001
*p=0.0313
vascular density
(% relative to ctrl)
Ctrl
Vehi
Beva
KDR2-2
H
****p<0.0001
****p<0.0001
ns
Vessel diameter (um)
Ctrl
Vehi
Beva
KDR2-2
D
Vehicle
Bevacizumab
KDR2-2
50
300
F
GLUT1
Ctrl
Vehicle
Bevacizumab
KDR2-2
200 μm

Figure 1. KDR2-2 is more effective than Bevacizumab at ameliorating brain lesions, perfusion, and vascular remodeling in Gamma Knife-irradiated mice

A, Schematic timeline illustrating the Gamma Knife irradiation, drug administration regimen, cranial MRI examination, and sample collection. **B,** Representative brain MRI (T1WI) showing the key lesion plane in mice treated with vehicle, Bevacizumab, or KDR2-2 post-irradiation. **C,** Statistical comparison of brain lesion volumes across treatment groups (Mean ± SEM, AVOVA, n=5). **D,** Cortical blood flow (laser speckle imaging) and ROIs in mice treated with Vehicle, Bevacizumab, or KDR2-2. **E,** Quantitative analysis of blood flow perfusion in ROIs (Mean ± SEM, AVOVA, n=5 per group). **F,** Representative immunofluorescence images of brain endothelial in different groups. Scale bar = 200 μm. **G,** Statistical comparison of vascular density (Mean ± SEM). **H,** Statistical comparison of vascular diameter (Mean ± SEM).

2. KDR2-2 is superior to bevacizumab in mitigating glial activation, neuronal loss, and fibrinogen leakage

Neuroinflammation plays a critical role in RIBI, primarily mediated by microglia, astrocytes, and peripheral immune cells. We therefore investigated whether KDR2-2 could attenuate the cerebral inflammatory response in this setting. Multiplex immunofluorescence staining revealed distinct patterns of astrocyte and microglial activation across the three groups (Fig. 2A).Quantitative analysis showed that Bevacizumab significantly reduced GFAP intensity compared to Vehicle (Fig. 2B, $P<0.0001$), indicating suppressed astrocyte activation. KDR2-2 further enhanced this suppression, exhibiting a greater reduction in GFAP intensity than Bevacizumab (Fig. 2B, $P<0.0001$). In contrast, both Bevacizumab and KDR2-2 significantly decreased IBA1 intensity relative to Vehicle (Fig. 2C, $P<0.0001$), with no statistically significant difference between the two treatments (Fig. 2C, $P=0.0503$). Thus, KDR2-2 more effectively mitigates astrocyte-mediated neuroinflammation than Bevacizumab, while exerting a comparable effect on microglial activation.

In addition to inducing glial activation, radiation directly causes neuronal DNA damage

and negatively regulates DNA repair mechanisms and neuroprotective pathways, thereby promoting neuronal degeneration[34]. We therefore assessed whether pharmacological intervention could mitigate neuronal injury in Gamma Knife-irradiated mice. Immunofluorescence staining for NeuN (neurons) and DAPI (nuclei) revealed the lowest NeuN intensity and neuronal survival in Vehicle-treated mice (Fig. 2D). Both Bevacizumab and KDR2-2 treatments significantly increased NeuN intensity and improved neuronal survival compared to Vehicle (Fig. 2E, $P<0.0001$), indicating that both therapies effectively ameliorate radiation-induced neuronal loss.

Finally, we assessed whether KDR2-2 mitigates vascular leakage following radiation injury. MIF co-staining for CD31 (endothelium), fibrinogen, and DAPI were used to evaluate cerebrovascular leakage across four groups: normal, Gamma Knife-irradiated mice treated with Vehicle, Bevacizumab, or KDR2-2. Vehicle-treated irradiated mice exhibited the highest fibrinogen intensity, indicating severe vascular leakage (Fig. 2F). Both Bevacizumab and KDR2-2 treatments markedly reduced fibrinogen extravasation (Fig. 2F). Quantification confirmed significantly elevated fibrinogen intensity in the Vehicle group compared to normal mice (Fig. 2G, $P < 0.0001$). In contrast, fibrinogen intensity in both the Bevacizumab- and KDR2-2-treated groups decreased significantly and was restored to levels statistically comparable to those in normal mice (Fig. 2G).

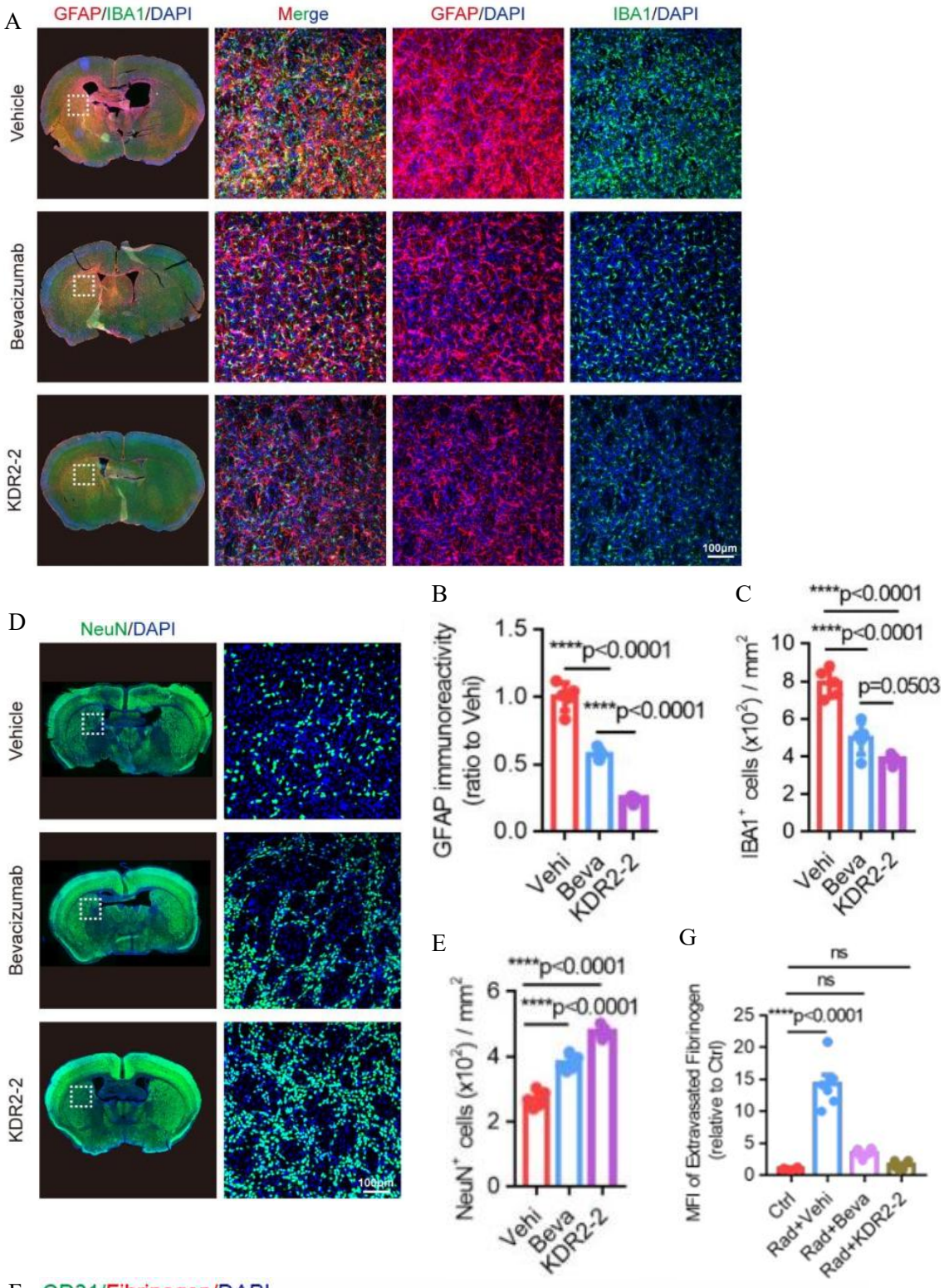

A
GFAP/IBA1/DAPI
Merge
GFAP/DAPI
IBA1/DAPI
Vehicle
Bevacizumab
KDR2-2
100μm
B
GFAP immunoreactivity (ratio to Vehi)
****p<0.0001
****p<0.0001
Vehi
Beva
KDR2-2
C
IBA1+ cells (x10²) / mm²
****p<0.0001
****p<0.0001
p=0.0503
D
NeuN/DAPI
E
NeuN+ cells (x10²) / mm²
****p<0.0001
****p<0.0001
G
MFI of Extravasated Fibrinogen (relative to Ctrl)
ns
ns
****p<0.0001
Ctrl
Rad+Vehi
Rad+Beva
Rad+KDR2-2
F
CD31/Fibrinogen/DAPI
Ctrl
Vehicle
Bevacizumab
KDR2-2
200 μm

Figure 2. KDR2-2 is more effective than Bevacizumab at alleviating gliosis, neuronal loss and fibrinogen exudation after radiation

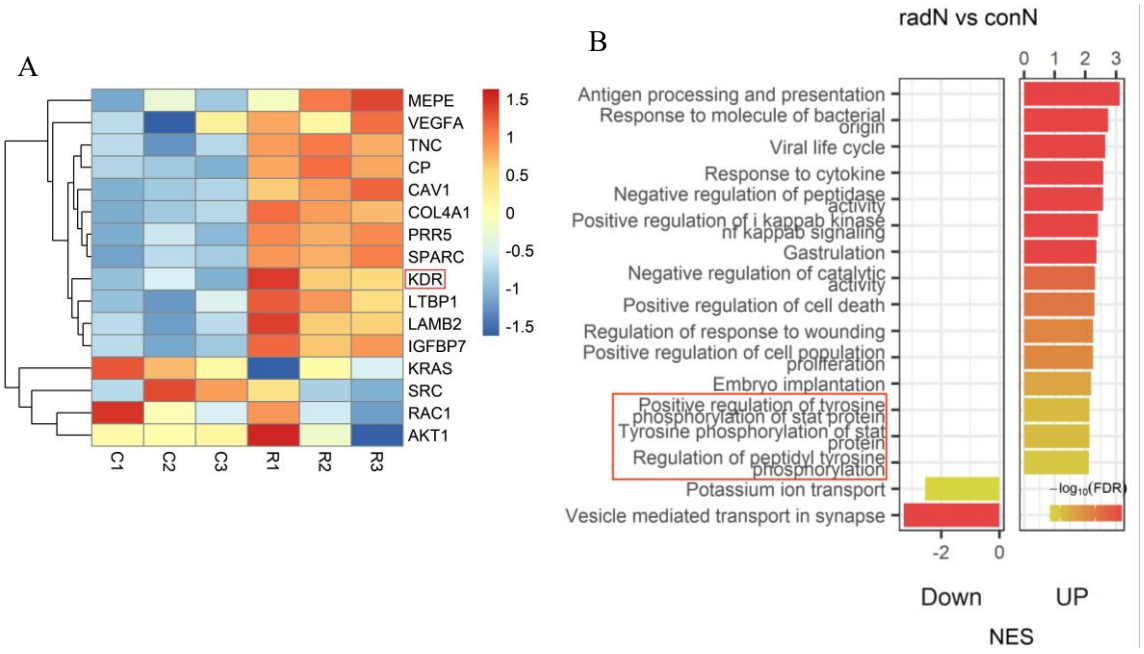
A, Representative images of $GFAP^+$ and $IBA1^+$ glial cells in mouse brain sections from different treatment groups. Scale bar = 100 μm. **B,** Statistical comparison of GFAP fluorescence intensity (Mean ± SEM, AVOVA, n=5). **C,** Statistical comparison of IBA1 fluorescence intensity (Mean ± SEM, AVOVA, n=5). **D,** Representative images of NeuN+ neurons (green) from different treatment groups. DAPI (blue) stains nuclei. Scale bar = 100 μm. **E,** Statistical comparison of NeuN fluorescence intensity (Mean ± SEM, AVOVA, n=5). **F,** Representative images of fibrinogen leakage and blood vessels in different groups. Scale bar = 200 μm. **G,** Statistical comparison of Fibrinogen fluorescence intensity (Mean ± SEM, AVOVA, n=7).

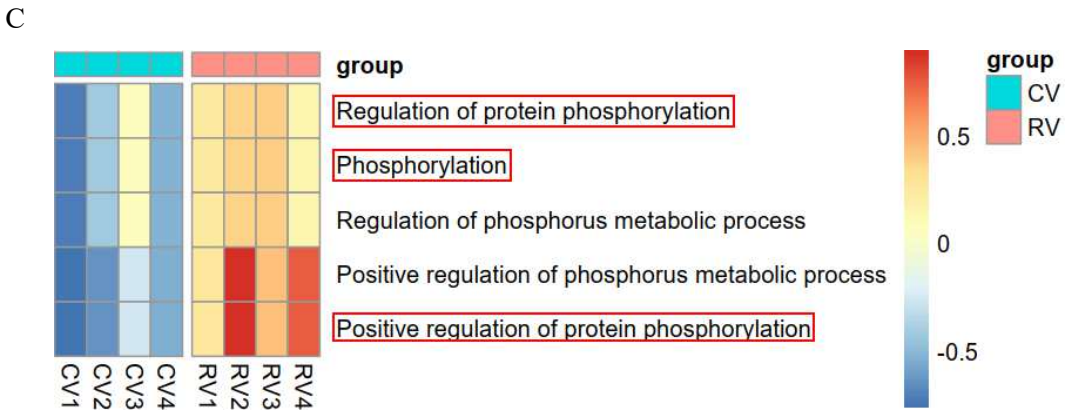
3. Bulk RNA sequencing demonstrates upregulation of VEGFR2 and its downstream phosphorylation signaling in RIBI

KDR2-2 outperforms bevacizumab in ameliorating cerebral pathology, highlighting pivotal role of VEGFR2 in RIBI. VEGFR2 is selectively expressed in vascular endothelial cells and signals only after ligand-triggered phosphorylation on specific tyrosine residues. To determine the role of VEGFR2 phosphorylation in RIBI, we generated a transcriptomic heatmap of phosphorylation-related genes from bulk RNA-seq data of RIBI and non-RIBI human specimens (Fig. 3A). Transcriptomic analysis revealed profound upregulation of phosphorylation-related genes (MEPE, TNC, CP, COL4A1, SPARC, LTBP1, IGFBP7) in RIBI patients, along with elevated expression of VEGFA and its receptor VEGFR2 (encoded by gene KDR, Fig. 3A). Concurrent upregulation of CAV1 and PRR5 are associated with VEGFR2-mediated vascular permeability (Fig. 3A). Functional enrichment highlighted significant over-representation of tyrosine-phosphorylation signatures (Fig. 3B).

To assess cross-species concordance, GSVA was applied to γ-knife mouse RNA-seq data using phosphorylation-related Gene Ontology biological process terms. Phosphorylation-related pathways were significantly enriched in irradiated mice compared to controls (Fig. 3C). Among VEGFR family members, only KDR was significantly upregulated post-

irradiation (Fig. 3D, P=0.029), whereas FLT1 (VEGFR1) and FLT4 (VEGFR3) remained unchanged. These results collectively demonstrate consistent VEGFR2 elevation and phosphorylation pathway activation in both RIBI patients and γ-Knife-irradiated mice.


A
MEPE
VEGFA
TNC
CP
CAV1
COL4A1
PRR5
SPARC
KDR
LTBP1
LAMB2
IGFBP7
KRAS
SRC
RAC1
AKT1
C1
C2
C3
R1
R2
R3
1.5
1
0.5
0
-0.5
-1
-1.5
B
radN vs conN
Antigen processing and presentation
Response to molecule of bacterial origin
Viral life cycle
Response to cytokine
Negative regulation of peptidase activity
Positive regulation of i kappab kinase nf kappab signaling
Gastrulation
Negative regulation of catalytic activity
Positive regulation of cell death
Regulation of response to wounding
Positive regulation of cell population proliferation
Embryo implantation
Positive regulation of tyrosine phosphorylation of stat protein
Tyrosine phosphorylation of stat protein
Regulation of peptidyl tyrosine phosphorylation
Potassium ion transport
Vesicle mediated transport in synapse
0 1 2 3
-2 0
-log10(FDR)
Down
UP
NES


C
group
Regulation of protein phosphorylation
Phosphorylation
Regulation of phosphorus metabolic process
Positive regulation of phosphorus metabolic process
Positive regulation of protein phosphorylation
CV1
CV2
CV3
CV4
RV1
RV2
RV3
RV4
group
CV
RV
0.5
0
-0.5

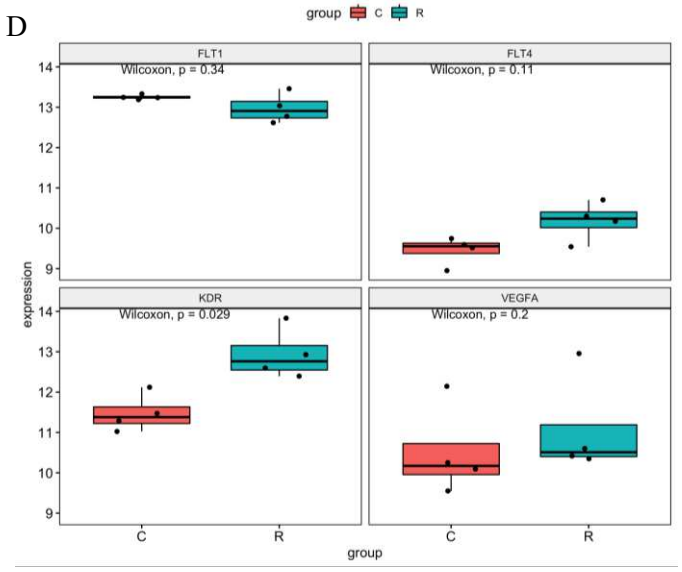

D
group C R
FLT1
Wilcoxon, p = 0.34
FLT4
Wilcoxon, p = 0.11
KDR
Wilcoxon, p = 0.029
VEGFA
Wilcoxon, p = 0.2
expression
14
13
12
11
10
9
C
R
group

Figure 3. Bulk RNA sequencing of RIBI patients and mice revealed upregulation of VEGFR2 and its associated phosphorylation signaling pathway

A, Heatmap of differentially expressed phosphorylation-related genes in bulk sequencing of brain tissue from RIBI patients vs. control group. **B,** GO-GSEA functional enrichment analysis of differentially expressed genes in RIBI patients vs. control group. **C,** GSVA enrichment scores for phosphorylation-related GOBP pathways in brain tissue of γ-knife mice vs. normal control mice. **D,** Box plot of differentially expressed VEGFR-related genes in γ-knife mice vs. normal control mice.

4. Phosphoprotein array reveals radiation-induced VEGFR2 Y1214 and HSP90β S226 hyperphosphorylation in endothelial cells

Phosphorylation of VEGFR2 at tyrosine Y949 (corresponding to human Y951) is primarily linked to increased vascular permeability, while phosphorylation at Y1173 (human Y1175) is associated with angiogenesis[35]. However, VEGFR2 pY949 and VEGFR2 pY1173 remained unchanged in irradiated bEND.3 cells compared to controls, showing no significant differences (Supple Fig. 2A-D; P=0.1163 and P=0.1198, respectively).

Based on the absence of increased phosphorylation at previously reported vascular leakage-associated sites following radiation, we hypothesized that RIBI-induced vascular hyperpermeability might involve a relatively specific VEGFR2 phosphorylation site. We therefore profiled phosphorylation changes in irradiated versus non-irradiated bEND.3 cells using a CSP100Plus antibody microarray (Fig. 4A). Scanning results indicated upregulation of phosphorylated VEGFR2 Y1214 post-irradiation (Fig. 4A, solid blue box), whereas total VEGFR2 levels remained comparable between groups (Fig. 4A, dashed blue box). The most prominently increased phosphorylation was observed at serine 226 of heat shock protein 90β (HSP90β S226) (Fig. 4A, solid red box), with no concomitant increase in total HSP90β (Fig. 4A, dashed red box). Corresponding changes were visualized in a heatmap based on Log2 Fold Change values (Fig. 4B). Pathway enrichment analysis of differentially phosphorylated proteins revealed significant activation of the VEGF signaling pathway in irradiated cells,

indicating VEGFR2 activation and subsequent upregulation of the downstream PI3K-AKT pathway (Fig. 4C).

Then the key phospho-targets identified by microarray were validated through western blot across multiple models. Phosphorylation of VEGFR2 Y1214 was significantly increased in irradiated bEND.3 cells (Supple Fig. 3A, P=0.0294), Gamma Knife-irradiated mice (Supple Fig. 3B, P=0.0434), and human RIBI lesion cores (R0) compared to distal regions (R2) (Fig. 4D and E, P=0.0385). Similarly, HSP90β S226 phosphorylation was markedly elevated in irradiated bEND.3 cells (Supple Fig. 3C, P=0.0037), Gamma Knife-irradiated mice (Supple Fig. 3D, P=0.0018), and human RIBI lesion cores (Fig. 4F and G, P=0.0389), confirming its consistent upregulation after irradiation.

Another two known phosphorylation sites in the irradiated bEND.3 cell model were evaluated. No significant alteration in phosphorylation was observed at VEGFR2 Y1054 (Supple Fig. 4A, P=0.2925) or Y996 (Supple Fig. 4B, P=0.1232) following irradiation compared to non-irradiated controls.

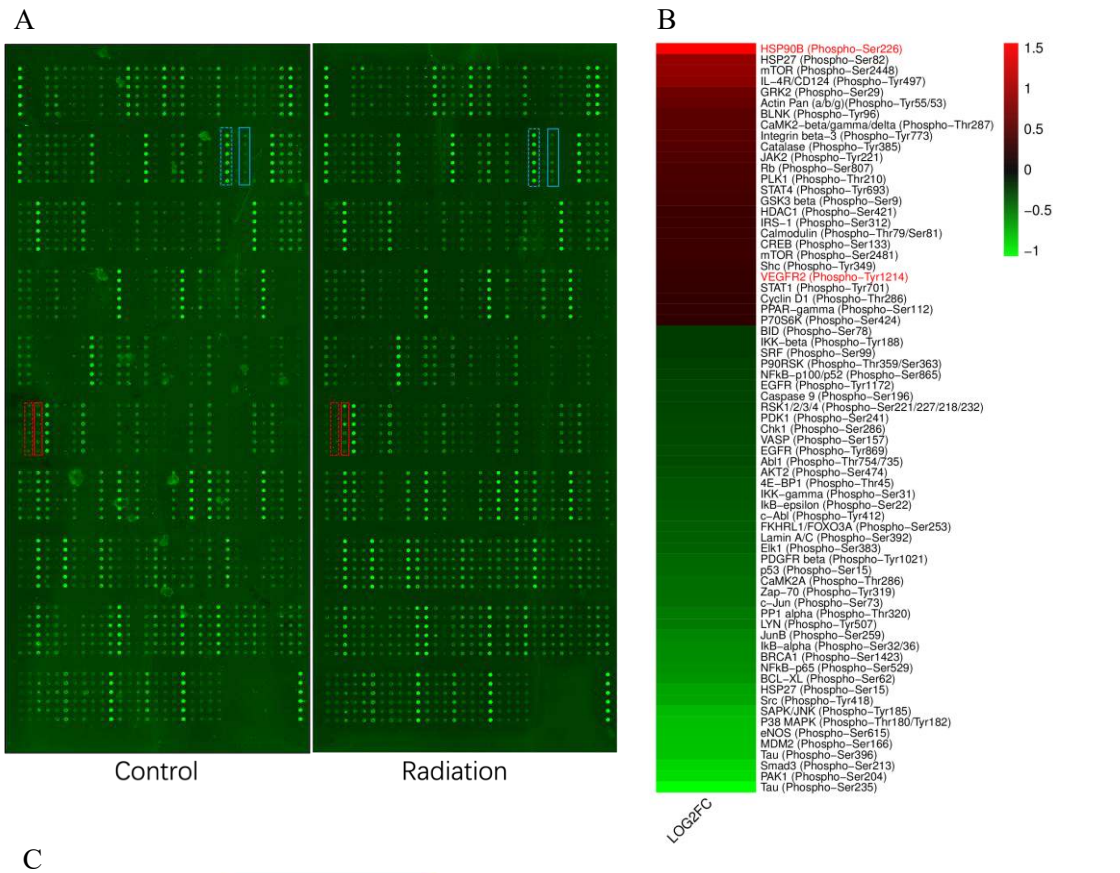

A
Control
Radiation
B
HSP90B (Phospho−Ser226)
HSP27 (Phospho−Ser82)
mTOR (Phospho−Ser2448)
IL−4R/CD124 (Phospho−Tyr497)
GRK2 (Phospho−Ser29)
Actin Pan (a/b/g)(Phospho−Tyr55/53)
BLNK (Phospho−Tyr96)
CaMK2−beta/gamma/delta (Phospho−Thr287)
Integrin beta−3 (Phospho−Tyr773)
Catalase (Phospho−Tyr385)
JAK2 (Phospho−Tyr221)
Rb (Phospho−Ser807)
PLK1 (Phospho−Thr210)
STAT4 (Phospho−Tyr693)
GSK3 beta (Phospho−Ser9)
HDAC1 (Phospho−Ser421)
IRS−1 (Phospho−Ser312)
Calmodulin (Phospho−Thr79/Ser81)
CREB (Phospho−Ser133)
mTOR (Phospho−Ser2481)
Shc (Phospho−Tyr349)
VEGFR2 (Phospho−Tyr1214)
STAT1 (Phospho−Tyr701)
Cyclin D1 (Phospho−Thr286)
PPAR−gamma (Phospho−Ser112)
P70S6K (Phospho−Ser424)
BID (Phospho−Ser78)
IKK−beta (Phospho−Tyr188)
SRF (Phospho−Ser99)
P90RSK (Phospho−Thr359/Ser363)
NFkB−p100/p52 (Phospho−Ser865)
EGFR (Phospho−Tyr1172)
Caspase 9 (Phospho−Ser196)
RSK1/2/3/4 (Phospho−Ser221/227/218/232)
PDK1 (Phospho−Ser241)
Chk1 (Phospho−Ser286)
VASP (Phospho−Ser157)
EGFR (Phospho−Tyr869)
Abl1 (Phospho−Thr754/735)
AKT2 (Phospho−Ser474)
4E−BP1 (Phospho−Thr45)
IKK−gamma (Phospho−Ser31)
IkB−epsilon (Phospho−Ser22)
c−Abl (Phospho−Tyr412)
FKHRL1/FOXO3A (Phospho−Ser253)
Lamin A/C (Phospho−Ser392)
Elk1 (Phospho−Ser383)
PDGFR beta (Phospho−Tyr1021)
p53 (Phospho−Ser15)
CaMK2A (Phospho−Thr286)
Zap−70 (Phospho−Tyr319)
c−Jun (Phospho−Ser73)
PP1 alpha (Phospho−Thr320)
LYN (Phospho−Tyr507)
JunB (Phospho−Ser259)
IkB−alpha (Phospho−Ser32/36)
BRCA1 (Phospho−Ser1423)
NFkB−p65 (Phospho−Ser529)
BCL−XL (Phospho−Ser62)
HSP27 (Phospho−Ser15)
Src (Phospho−Tyr418)
SAPK/JNK (Phospho−Tyr185)
P38 MAPK (Phospho−Thr180/Tyr182)
eNOS (Phospho−Ser615)
MDM2 (Phospho−Ser166)
Tau (Phospho−Ser396)
Smad3 (Phospho−Ser213)
PAK1 (Phospho−Ser204)
Tau (Phospho−Ser235)
1.5
1
0.5
0
−0.5
−1
LOG2FC
C
ErbB signaling pathway
PI3K−Akt signaling pathway
MAPK signaling pathway
Focal adhesion
Apoptosis
Insulin signaling pathway
Ras signaling pathway
VEGF signaling pathway
mTOR signaling pathway
AMPK signaling pathway
NF−kappa B signaling pathway
p53 signaling pathway
Cell cycle
Autophagy − animal
JAK−STAT signaling pathway
TGF−beta signaling pathway
0
10
20
30
Count
Fold Enrichment
D
VEGFR2 pY1214
152kDa
VEGFR2 Total
230kDa
β-actin
42kDa
R2
R0
F
HSP90β pS226
90kDa
HSP90β Total
90kDa
β-actin
42kDa
R2
R0
G
0.0389
HSP90β pS226 Relative Expression
1.2
0.8
0.4
R2
R0
E
0.0385
VEGFR2 pY1214 Relative Expression
3
2
1
0
R2
R0

Figure 4. Phospho-antibody microarray revealed phosphorylation of VEGFR2 at Y1214 in bEND.3 cells following irradiation

A, Representative protein array image of Vegfr2 Y1214 phosphorylation (solid blue box) *vs.* Vegfr2 Total (dashed blue box), and Hsp90β S226 phosphory- lation (solid red box) *vs.* Hsp90β Total (dashed red box) in bEND.3 irradiated *vs.* control cells. **B,** Heatmap of differentially expressed phosphoproteins in irradiated bEND.3 cells *vs.* control. **C,** Signaling pathway enrichment analysis of differentially expressed genes in irradiated bEND.3 cells *vs.* control. **D,** VEGFR2 Y1214 phosphorylation in human RIBI specimens with representative blots. **E,** VEGFR2 pY1214/VEGFR2 ratio quantification (Mean ± SEM, n=4). **F,** HSP90β S226 phosphorylation in human RIBI specimens with representative blots. **G,** HSP90β pS226/ HSP90β ratio quantification (Mean ± SEM, n=4).

5. HSP90β potentiates radiation-induced vascular hyperpermeability via VEGFR2 Y1214 phosphorylation-dependent actin cytoskeletal remodeling

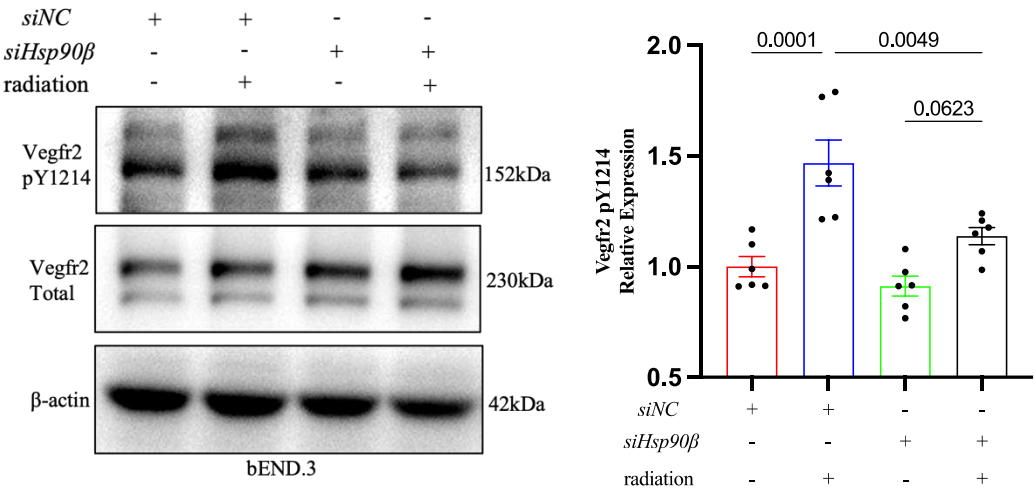
Given that HSP90β has been reported to promote endothelial-dependent angiogenesis in hepatocellular carcinoma by upregulating VEGFR1 and VEGFR2 expression[36], and based on our previous findings that radiation induces phosphorylation of both HSP90β S226 and VEGFR2 Y1214, we investigated whether HSP90β promotes VEGFR2 Y1214 phosphorylation in RIBI. Knockdown of Hsp90β in bEND.3 cells using specific siRNA resulted in an approximately 75% reduction in Hsp90β mRNA levels compared to the negative control siRNA (siNC) (Supple Fig. 5A, $P<0.001$). A positive control siRNA targeting Gapdh decreased its mRNA by approximately 80% (Supple Fig. 5B, $P < 0.01$), confirming transfection efficiency. Western blot analysis further demonstrated significant reduction of Hsp90β protein expression under both normal and irradiated conditions following siHsp90β transfection (Supple Fig. 5C and 5D, $P < 0.001$).

We next examined whether Hsp90β knockdown attenuates radiation-induced VEGFR2 Y1214 phosphorylation in endothelial cells. In cells transfected with control siRNA (siNC), irradiation significantly increased VEGFR2 Y1214 phosphorylation (Fig. 5A; $P=0.0001$). In

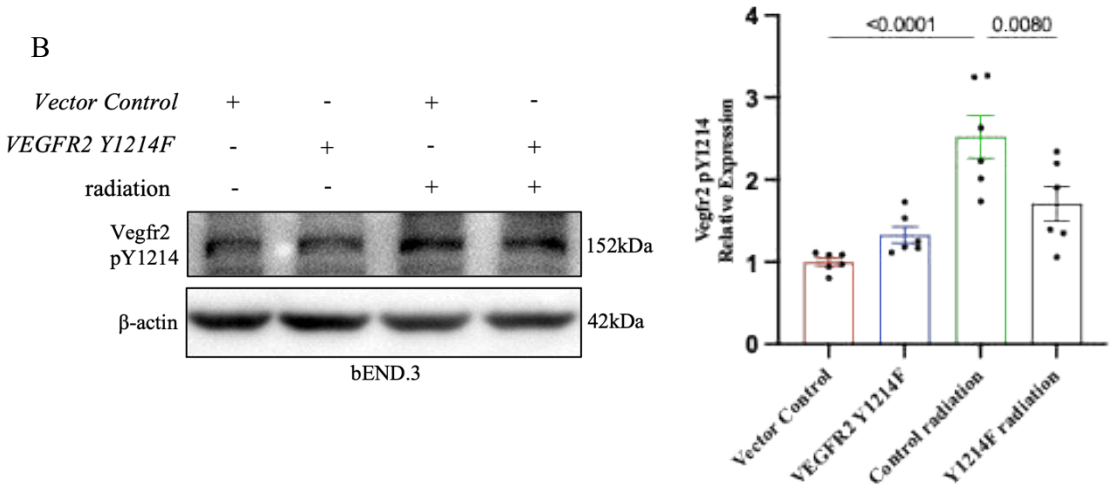
contrast, Hsp90β knockdown markedly suppressed this radiation-induced VEGFR2 pY1214(Fig. 5A; P=0.0049). These results indicate that Hsp90β promotes VEGFR2 Y1214 phosphorylation through a VEGFA-independent pathway, and that Hsp90β depletion significantly reduces VEGFR2 activation following irradiation.

It has been established that VEGFR2 Y1214 phosphorylation is required for SAPK2/p38-mediated actin remodeling in VEGF-exposed endothelial cells, a process that induces vascular leakage[22]. To determine the role of this specific phosphorylation event in cytoskeletal dynamics without VEGF, we generated the phosphorylation-deficient VEGFR2 mutant, Y1214F. BEND.3 cells were transfected with either a vector control plasmid or the VEGFR2 Y1214F mutant plasmid, followed by irradiation. Western blotting confirmed that while irradiation robustly increased pY1214 levels in the vector-transfected cells, phosphorylation was virtually diminished in the Y1214F mutant group (Fig. 5B). We then assessed the functional consequence of blocking this phosphorylation on the actin cytoskeleton. Immunofluorescence staining for F-actin revealed that the control cells subjected to irradiation exhibited marked cytoskeletal damage, with reduced overall actin levels and a fragmented, irregular arrangement (Fig. 5C). In contrast, irradiated cells expressing the VEGFR2 Y1214F mutant maintained significantly higher actin levels compared to the irradiated vector control. Furthermore, the F-actin fibers in the Y1214F mutant displayed a more organized pattern. This morphological evidence suggests that phosphorylation of VEGFR2 at Y1214 is the necessary and critical molecular switch that triggers radiation-induced actin cytoskeletal breakdown and subsequent endothelial barrier dysfunction.

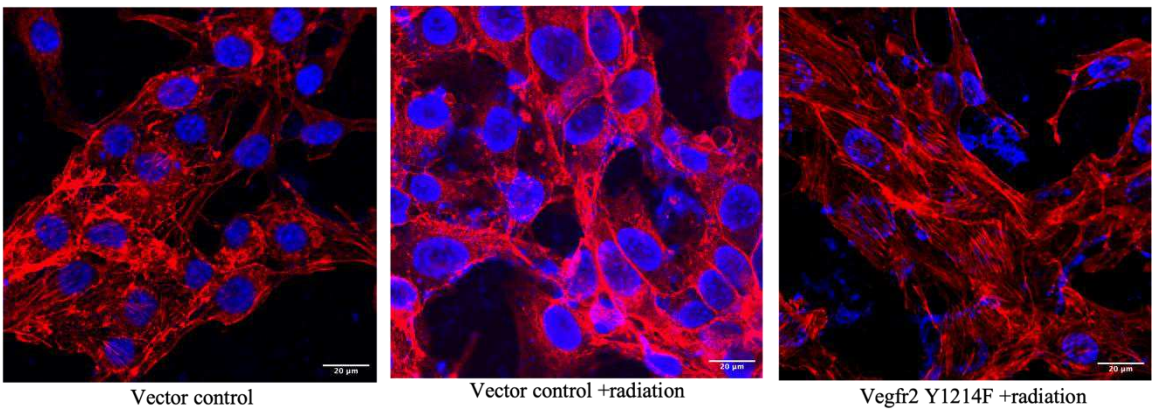
A



B



C



Vector control | Vector control +radiation | Vegfr2 Y1214F +radiation

Figure 5. HSP90β potentiates radiation-induced vascular hyperpermeability via VEGFR2 Y1214-mediated actin remodeling

A, Western blots of bEND.3 cells with siNC or siHsp90β siRNA prior to irradiation(left) and p-VEGFR2 (Y1214)/VEGFR2 ratio quantification (right) (Mean ± SEM, n=6). **B,** Western blots of bEND.3 cells with Vector Control or VEGFR2 Y1214F mutant prior to irradiation(left) and p-VEGFR2 (Y1214)/VEGFR2 ratio quantification (right) (Mean ± SEM, n=6). **C,** Representative immunofluorescence images of F-actin cytoskeleton organization in irradiated bEND.3 cells transfected with Vector Control or VEGFR2 Y1214F mutant.

Discussion

RIBI represents a severe complication of radiotherapy, characterized by cognitive dysfunction and irreversible brain necrosis. Vascular injury is widely recognized as a central driver of this radiation-induced CNS toxicity[37-38]. Due to the irreversibility of RIBI, current clinical treatments------including corticosteroids, bevacizumab, antiplatelet agents, and hyperbaric oxygen------offer limited efficacy[39-41]. There is an urgent need to explore novel therapeutic agents for patients unresponsive to standard care. In this study, we identify KDR2-2 as a potent inhibitor that markedly attenuates pathological features in a Gamma knife irradiation mouse model. Furthermore, combined RNA sequencing and phosphoprotein profiling reveal that radiation induces VEGFR2 Y1214 and HSP90β S226 phosphorylation in endothelial cells. Crucially, we demonstrate that HSP90β mediates VEGFR2 activation via a VEGF-independent, non-classical mechanism.

RIBI induces VEGFA upregulation, activating the VEGF/VEGFR pathway which mediates developmental vasculogenesis, pathological angiogenesis, and vascular permeability[35]. Numerous agents targeting VEGF signaling have been developed and are used to treat various cancers and neovascular ocular diseases[42]. While VEGF inhibitors like bevacizumab are used for RIBI[43-44], their irreversible blockade of angiogenesis can exacerbate hypoxia, upregulate HIF-1α, and trigger a vicious cycle of aberrant VEGF-driven vascular leakage, edema, and radionecrosis recurrence[8]. Furthermore, bevacizumab only indirectly modulates VEGFR2, and multi-targeted TKIs (like sunitinib, sorafenib) have toxicity issues, driving the development of selective VEGFR2 agents[42].

KDR2-2, a novel VEGFR2-targeting inhibitor, has demonstrated anti-neovascular effects with a favorable safety profile in preclinical studies and Phase I clinical trial (NCT04620109). It has now entered a Phase I clinical trial in China as a non-invasive candidate for neovascular glaucoma (NCT04844619). Our investigation shows that KDR2-2 inhibits VEGFR2 expression in endothelial cells more potently than apatinib or cabozantinib. In our murine RIBI model, KDR2-2 treatment significantly reduced edema and normalized vascular density and morphology. These structural improvements restored cerebral perfusion, reduced fibrinogen leakage and immune infiltration, and attenuated neuroinflammation. The fact that

the selective VEGFR2 apatinib did not outperform bevacizumab in our in vitro assays or prior clinical reports suggests further inquiry[13].

Mechanistically, VEGFR2 is activated via site-specific phosphorylation, our bulk RNA-seq data implicated this post-translational modification in RIBI. While Y949 and Y1173 are known to regulate leakage and angiogenesis, respectively, our in vitro analysis showed no changes at these sites[35]. Instead, a phospho-protein array revealed specific radiation-induced phosphorylation at VEGFR2 Y1214 and HSP90β S226, associated with PI3K-AKT pathway upregulation[45]. Since VEGFR2 can be activated by non-canonical mechanisms[17,18], we propose that radiation triggers upstream signaling that phosphorylates VEGFR2 at Y1214. This hypothesis is supported by the superior efficacy of KDR2-2 over bevacizumab. Bevacizumab blocks only VEGFA binding, leaving other phosphorylation mechanisms unchecked. These alternative activators likely sustain VEGFR2 signaling, driving disease progression.

HSP90, a molecular chaperone, maintains proteostasis by mediating folding, refolding, maturation, and the disassembly and degradation of protein aggregates[46]. Its abundance increases from 1–2% under basal conditions to 4–6% under stress[47]. Our study reveals a previously unreported role for HSP90β in promoting VEGFR2 Y1214 phosphorylation post-irradiation. We postulate that radiation upregulates HSP90β and enhances its phosphorylation at S226, strengthening its binding to co-chaperones and its client protein VEGFR2, ultimately driving Y1214 phosphorylation[48]. Conversely, activated VEGFR2 may induce HSP90β tyrosine phosphorylation, a process that depends on VEGFR2 internalization and Src kinase activation in response to VEGF[49], suggesting a potential positive feedback cycle. Previous studies have established that VEGFR2 mediates VEGF-induced cell migration by coordinating the SAPK2/p38 pathway for actin polymerization and the HSP90/FAK axis for focal adhesion and stress fiber assembly[50]. Our results further identified VEGFR2 Y1214 phosphorylation as the critical event triggering actin rearrangement.

In summary, our study identifies KDR2-2 as a promising neuroprotective agent against RIBI. We reveals VEGFR2 Y1214 phosphorylation as the key activation mechanism in radiation-induced VEGFR2 activation. We uncovers that HSP90β induces VEGFR2 Y1214

phosphorylation via a non-canonical, VEGFA-independent pathway. Given that KDR2-2 is progressing to phase 1 clinical trials for neovascular glaucoma, our results provide a promising candidate drug for treating RIBI patients unsuitable for glucocorticoid and bevacizumab therapies.

A primary limitation of this study is the absence of animal experiments investigating HSP90β-targeted therapy for RIBI. Subsequent research will involve treating Gamma Knife mice with specific HSP90β inhibitors to assess their in vivo efficacy and to further define the functional contribution of the HSP90β–VEGFR2 Y1214 signaling axis.

Data availability

The authors confirm that the data supporting the findings of this study are available within the article and its Supplementary materials.

Acknowledgements

We are deeply grateful to Wei-Jye Lin for his constant guidance throughout the experimental work.

Funding

This work was supported by grants from the STI 2030 Major Projects (2022ZD0211603), the National Natural Science Foundation of China (82330099, 82530100), the Key Area Research and Development Program of Guangdong Province (2023B0303040003), and the Science and Technology Program of Guangzhou (2023A03J0708) to Yamei Tang.

Competing interests

The authors declare no potential conflicts of interest.

References

[1] Zhang Q, Liang J, Li X, et al. Exploring antithrombotic mechanisms and effective constituents of Lagopsis supina using an integrated strategy based on network pharmacology, molecular docking, metabolomics, and experimental verification in rats. J Ethnopharmacol, 2025,336:118717.

[2] Van den Bosch L, van der Laan HP, van der Schaaf A, et al. Patient-Reported Toxicity and Quality-of-Life Profiles in Patients With Head and Neck Cancer Treated With Definitive Radiation Therapy or Chemoradiation. Int J Radiat Oncol Biol Phys, 2021,111(2):456-467.

[3] Zhang YM, Kang YF, Zeng JJ, et al. Surface-Based Falff: A Potential Novel Biomarker for Prediction of Radiation Encephalopathy in Patients With Nasopharyngeal Carcinoma. Front Neurosci, 2021,15:692575.

[4] Wang TM, Shen GP, Chen MY, et al. Genome-Wide Association Study of Susceptibility Loci for Radiation-Induced Brain Injury. J Natl Cancer Inst, 2019,111(6):620-628.

[5] Béhin A, Delattre JY. Complications of radiation therapy on the brain and spinal cord. Semin Neurol, 2004,24(4):405-417.

[6] Nonoguchi N, Miyatake S, Fukumoto M, et al. The distribution of vascular endothelial growth factor-producing cells in clinical radiation necrosis of the brain: pathological consideration of their potential roles. J Neurooncol, 2011,105(2):423-431.

[7] Kamiryo T, Lopes MB, Kassell NF, Steiner L, Lee KS. Radiosurgery-induced microvascular alterations precede necrosis of the brain neuropil. Neurosurgery, 2001,49(2):409-414; discussion 414-405.

[8] Miyatake S, Nonoguchi N, Furuse M, et al. Pathophysiology, diagnosis, and treatment of radiation necrosis in the brain. Neurol Med Chir (Tokyo), 2015,55(1):50-59.

[9] Zhuang H, Shi S, Yuan Z, Chang JY. Bevacizumab treatment for radiation brain necrosis: mechanism, efficacy and issues. Mol Cancer, 2019,18(1):21.

[10] Zhuang H, Yuan X, Sun D, et al. Acquired-resistance of bevacizumab treatment for radiation brain necrosis: a case report. Oncotarget, 2016,7(11):13265-13268.

[11] Liu Y, Li Y, Wang Y, Lin C, Zhang D, Chen J, et al. Recent progress on vascular endothelial growth factor receptor inhibitors with dual targeting capabilities for tumor therapy. J Hematol Oncol. 2022;15(1):89. doi: 10.1186/s13045-022-01310-7

[12] Jang S, Strickland B, Finis L, et al. Comparative biochemical kinase activity analysis identifies rivoceranib as a highly selective VEGFR2 inhibitor. Cancer Chemother Pharmacol, 2023,91(6):491-499.

[13] He L, Pi Y, Li Y, et al. Efficacy and Safety of Apatinib for Radiation-induced Brain Injury Among Patients With Head and Neck Cancer: An Open-Label, Single-Arm, Phase 2 Study. Int J Radiat Oncol Biol Phys, 2022,113(4):796-804.

[14] Noda R, Akabane A, Kawashima M, et al. VEGFR-TKI treatment for radiation-induced brain injury after gamma knife radiosurgery for brain metastases from renal cell carcinomas. Jpn J Clin Oncol, 2023,53(4):355-364.

[15] Jang S, Strickland B, Finis L, et al. Comparative biochemical kinase activity analysis identifies rivoceranib as a highly selective VEGFR2 inhibitor. Cancer Chemother Pharmacol, 2023,91(6):491-499.

[16] Lemmon MA, Schlessinger J. Cell signaling by receptor tyrosine kinases. Cell, 2010,141(7):1117-1134.

[17] Shibuya M. VEGFR and type-V RTK activation and signaling. Cold Spring Harb Perspect Biol, 2013,5(10):a009092.

[18] Simons M, Gordon E, Claesson-Welsh L. Mechanisms and regulation of endothelial VEGF receptor signalling. Nature Reviews Molecular Cell Biology, 2016,17(10):611-625.

[19] Koch S, Claesson-Welsh L. Signal transduction by vascular endothelial growth factor receptors. Cold Spring Harb Perspect Med, 2012,2(7):a006502.

[20] Zhou W, Liu K, Zeng L, et al. Targeting VEGF-A/VEGFR2 Y949 Signaling-Mediated Vascular Permeability Alleviates Hypoxic Pulmonary Hypertension. Circulation, 2022,146(24):1855-1881.

[21] Sjöberg E, Melssen M, Richards M, et al. Endothelial VEGFR2-PLCγ signaling regulates vascular permeability and antitumor immunity through eNOS/Src. J Clin Invest, 2023,133(20).

[22] Lamalice L, Houle F, Jourdan G, Huot J. Phosphorylation of tyrosine 1214 on VEGFR2 is required for VEGF-induced activation of Cdc42 upstream of SAPK2/p38. Oncogene, 2004,23(2):434-445.

[23] Zhuang T, Lei Y, Chang JJ, et al. A2AR-mediated lymphangiogenesis via VEGFR2 signaling prevents salt-sensitive hypertension. Eur Heart J, 2023,44(29):2730-2742.

[24] Jiang X, Engelbach JA, Yuan L, et al. Anti-VEGF antibodies mitigate the development of radiation necrosis in mouse brain. Clin Cancer Res, 2014,20(10):2695-2702.

[25] He B, Wang X, He Y, et al. Gamma ray-induced glial activation and neuronal loss occur before the delayed onset of brain necrosis. Faseb j, 2020,34(10):13361-13375.

[26] Jiang X, Yuan L, Engelbach JA, et al. A Gamma-Knife-Enabled Mouse Model of Cerebral Single-Hemisphere Delayed Radiation Necrosis. PLoS One, 2015,10(10):e0139596.

[27] Zhao Z, Johnson MS, Chen B, et al. Live-cell imaging to detect phosphatidylserine externalization in brain endothelial cells exposed to ionizing radiation: implications for the treatment of brain arteriovenous malformations. J Neurosurg, 2016,124(6):1780-1787.

[28] Raoufi-Rad N, McRobb LS, Lee VS, et al. In vivo imaging of endothelial cell adhesion molecule expression after radiosurgery in an animal model of arteriovenous malformation. PLoS One, 2017,12(9):e0185393.

[29] Liu S, Sammons V, Fairhall J, et al. Molecular responses of brain endothelial cells to radiation in a mouse model. J Clin Neurosci, 2012,19(8):1154-1158.

[30] Zhang X, Zhu M, Xie L, et al. Cabozantinib, a Multityrosine Kinase Inhibitor of MET and VEGF Receptors Which Suppresses Mouse Laser-Induced Choroidal Neovascularization. J Ophthalmol, 2020,2020:5905269.

[31] Koike S, Aida N, Hata M, Fujita K, Ozawa Y, Inoue T. Asymptomatic radiation-induced telangiectasia in children after cranial irradiation: frequency, latency, and dose relation. Radiology, 2004,230(1):93-99.

[32] Kralik SF, Watson GA, Shih CS, Ho CY, Finke W, Buchsbaum J. Radiation-Induced Large Vessel Cerebral Vasculopathy in Pediatric Patients With Brain Tumors Treated With Proton Radiation Therapy. Int J Radiat Oncol Biol Phys, 2017,99(4):817-824.

[33] Warrington JP, Csiszar A, Johnson DA, et al. Cerebral microvascular rarefaction induced by whole brain radiation is reversible by systemic hypoxia in mice. Am J Physiol Heart Circ Physiol, 2011,300(3):H736-744.

[34] Sabirzhanov B, Makarevich O, Barrett JP, et al. Irradiation-Induced Upregulation of miR-711 Inhibits DNA Repair and Promotes Neurodegeneration Pathways. Int J Mol Sci, 2020,21(15).

[35] Pérez-Gutiérrez L, Ferrara N. Biology and therapeutic targeting of vascular endothelial growth factor A. Nat Rev Mol Cell Biol, 2023,24(11):816-834.

[36] Meng J, Liu Y, Han J, et al. Hsp90β promoted endothelial cell-dependent tumor angiogenesis in hepatocellular carcinoma. Mol Cancer, 2017,16(1):72.

[37] Yang X, Ren H, Fu J. Treatment of Radiation-Induced Brain Necrosis. Oxid Med Cell Longev, 2021,2021:4793517.

[38] Chao ST, Ahluwalia MS, Barnett GH, Stevens GH, Murphy ES, Stockham AL, Shiue K, Suh JH. Challenges with the diagnosis and treatment of cerebral radiation necrosis. Int J Radiat Oncol Biol Phys. 2013;87:449–457. doi: 10.1016/j.ijrobp.2013.05.015

[39] Pan, D.; Rong, X.; Zhu, Y.; Ng, W. T.; Chen, D.; Li, H.; Xu, Y.;Tang, Y. A Novel Nomogram to Predict Overall Survival in Head and Neck Cancer Survivors with Radiation-Induced Brain Necrosis. Radiother. Oncol. 2022, 168, 121−129.

[40] Cai, J.; Zheng, J.; Shen, J.; Yuan, Z.; Xie, M.; Gao, M.; Tan, H.;Liang, Z.; Rong, X.; Li, Y.; Li, H.; Jiang, J.; Zhao, H.; Argyriou, A. A.;Chua, M.; Tang, Y. A Radiomics Model for Predicting the Response to Bevacizumab in Brain Necrosis After Radiotherapy. Clin. Cancer Res. 2020, 26, 5438−5447.

[41] Li, H.; Rong, X.; Hu, W.; Yang, Y.; Lei, M.; Wen, W.; Yue, Z.;Huang, X.; Chua, M.; Li, Y.; Cai, J.; He, L.; Pan, D.; Cheng, J.; Pi, Y.;Xue, R.; Xu, Y.; Tang, Y. Bevacizumab Combined with Cortico-steroids Does Not Improve the Clinical Outcome of Nasopharyngeal Carcinoma Patients with Radiation-Induced Brain Necrosis. Front.Oncol. 2021, 11, No. 746941

[42] Cao Y, Langer R, Ferrara N. Targeting angiogenesis in oncology, ophthalmology and beyond. Nat Rev Drug Discov, 2023,22(6):476-495.

[43] Zhuang H, Yuan X, Zheng Y, et al. A study on the evaluation method and recent clinical efficacy of bevacizumab on the treatment of radiation cerebral necrosis. Sci Rep, 2016,6:24364.

[44] Boothe D, Young R, Yamada Y, Prager A, Chan T, Beal K. Bevacizumab as a treatment for radiation necrosis of brain metastases post stereotactic radiosurgery. Neuro Oncol, 2013,15(9):1257-1263.

[45] Testini C, Smith RO, Jin Y, et al. Myc-dependent endothelial proliferation is controlled by phosphotyrosine 1212 in VEGF receptor-2. EMBO Rep, 2019,20(11):e47845.

[46] Biebl MM, Buchner J. Structure, Function, and Regulation of the Hsp90 Machinery. Cold Spring Harb Perspect Biol, 2019,11(9).

[47] Maiti S, Picard D. Cytosolic Hsp90 Isoform-Specific Functions and Clinical Significance. Biomolecules, 2022,12(9).

[48] Roychowdhury T, McNutt SW, Pasala C, et al. Phosphorylation-driven epichaperome assembly is a regulator of cellular adaptability and proliferation. Nature Communications, 2024,15(1):8912.

[49] Duval M, Le Boeuf F, Huot J, Gratton JP. Src-mediated phosphorylation of Hsp90 in response to vascular endothelial growth factor (VEGF) is required for VEGF receptor-2 signaling to endothelial NO synthase. Mol Biol Cell, 2007,18(11):4659-4668.

[50] Rousseau S, Houle F, Kotanides H, Witte L, Waltenberger J, Landry J, Huot J. Vascular endothelial growth factor (VEGF)-driven actin-based motility is mediated by VEGFR2 and requires concerted activation of stress-activated protein kinase 2 (SAPK2/p38) and geldanamycin-sensitive phosphorylation of focal adhesion kinase. J Biol Chem. 2000 Apr 7;275(14):10661-72.

Supplementary Files

This is a list of supplementary files associated with this preprint. Click to download.

- Supplementarymaterials.docx
- SupplementaryUncroppedGels.zip